IEEE Access
Multidisciplinary ⋮ Rapid Review ⋮ Open Access Journal

Received 13 January 2024, accepted 12 February 2024, date of publication 21 February 2024, date of current version 7 March 2024.

Digital Object Identifier 10.1109/ACCESS.2024.3368518

RESEARCH ARTICLE

NoQSM-net: Combining Convolutional Neural Network With Numerical Optimization Algorithm for Quantitative Susceptibility Mapping Reconstruction

QIANQIAN ZHANG[1,2], YIHAO GUO[3], AND WUFAN CHEN[1,2], (Senior Member, IEEE)
[1]School of Biomedical Engineering, Southern Medical University, Guangzhou 510515, China
[2]Guangdong Provincial Key Laboratory of Medical Image Processing, Guangzhou 510515, China
[3]Department of Radiology, Hainan General Hospital (Hainan Affiliated Hospital of Hainan Medical University), Haikou 570311, China

Corresponding author: Wufan Chen (chenwf@smu.edu.cn)

This work was supported in part by the Key-Area Research and Development Program of Guangdong Province under Grant 2018B030333001, in part by the National Natural Science Foundation of China under Grant 61971214, and in part by the Natural Science Foundation of Guangdong Province under Grant 2023A1515012093.

This work involved human subjects or animals in its research. Approval of all ethical and experimental procedures and protocols was granted by the Shanghai Jiao Tong University Human Ethics Committee.

ABSTRACT In gradient echo MRI, quantitative susceptibility mapping (QSM) quantifies the magnetic susceptibility distributions of tissues, which has great potential in detecting brain diseases. However, QSM reconstruction is an ill-conditional inversion problem because of the zeros in the frequency domain of the dipole kernel. The intrinsic nature of the ill-posedness would affect the accuracy of quantifying tissue susceptibility. Recently, deep learning-based methods have been proposed to improve accuracy by suppressing the streaking artifacts. In this work, we proposed a hybrid architecture to enforce data consistency by involving numerical optimization blocks within convolutional neural networks (CNN), which aimed to reconstruct high-quality QSM images, referred to as NoQSM-net. The Calculation of Susceptibility through Multiple Orientation Sampling (COSMOS) QSM maps were used as labels for training. The performance of the proposed method was evaluated on two healthy volunteers and brain images of patients with diseases. Our experiments showed that the proposed method achieved good performance in terms of quantitative metrics and could effectively suppress artifacts in reconstructed QSM images, demonstrating its potential for future applications. For experiments on patients with multiple sclerosis (MS), the proposed method could better detect lesion regions in the results of NoQSM-net.

INDEX TERMS Quantitative susceptibility mapping, dipole kernel inversion, MRI, numerical optimization, convolutional neural network.

I. INTRODUCTION

Magnetic susceptibility is an intrinsic and physical property that measures the degree of magnetization of matter when placed in an external magnetic field. Quantitative susceptibility mapping (QSM) is a comparatively advanced reconstruction technology that quantifies the magnetic susceptibility of local tissues. Some molecules and biomolecules are sensitive to susceptibility sources, such as hemoglobin, myelin, ferritin, and calcium. QSM has been applied to discriminate between hemorrhages and calcifications [1], [2], For neurological diseases, QSM can be used to quantify iron deposition, such as Alzheimer's disease, multiple sclerosis, Huntington's disease, and Parkinson's disease [3], [4], [5], [6]. In addition, QSM can be used to study cerebral microbleeds and intracranial hemorrhage [7], [8], [9], [10].

QSM reconstruction is an ill-conditioned inverse problem from the measurement field to the susceptibility source

The associate editor coordinating the review of this manuscript and approving it for publication was Eduardo Rosa-Molinar.

because of the zeroes in the Fourier domain of the dipole kernel, which are the source of noise and artifacts [11], [12]. Several approaches have been proposed to address this problem. One direct method is truncated k-space deconvolution (TKD), which can avoid the ill-conditioned problem by truncating the dipole kernel in k-space; however, the resulting QSM map suffers from streaking artifacts and noise [13]. To reduce artifacts and enhance the quality of QSM maps, a number of regularization algorithms have been addressed [14], [15], [16], [17], [18]. For example, the Morphology Enabled Dipole Inversion (MEDI) method has been proposed, which utilizes the structural consistency between the reconstructed susceptibility map and the corresponding magnitude image to reconstruct the QSM map [17]. However, certain errors such as artifacts induced by ill-posed inversion still exist. A more accurate QSM map can be reconstructed using the Calculation of Susceptibility through Multiple Orientation Sampling (COSMOS) algorithm [19], which is the gold standard for the single orientation QSM reconstruction method. Nevertheless, multiple head orientation scans prolong acquisition time, hindering their feasibility in clinical applications [20].

Recently, convolutional neural networks (CNN) based methods have been proposed to solve the ill-conditioned dipole inversion problem in QSM reconstruction by generating high-quality QSM images from single-orientation tissue field measurement [21], [22], [23], [24]. Most CNN-based methods are data-driven and heavily rely on the amount of data. For example, QSMnet [21], QSMnet+ [25] and DeepQSM [26] utilized 3D Unet to solve the ill-posed inversion problem. Reference [27] used an interactively connected clique U-Net (named ICCU-Net) for QSM reconstructiuon. And [28] proposed a SWI-to-QSM-Net (S2Q-Net) to reconstruct QSM images from Susceptibility weighted imaging (SWI) high-pass filtered phase data. xQSM [29] adopted an enhanced 3D Unet, and [24] used Generative Adversarial Networks (GANs) for dipole inversion. In addition, autoQSM [30] directly reconstructed QSM images from the total tissue phase. In addition to simple data-driven learning, [31] combined a variational network with a nonlinear model (VaNDI), which was trained to optimize regularizers in the Nonlinear Dipole Inversion (NDI) gradient update rule. In addition, a few methods incorporated the underlying physical model into CNN, such as Learned Proximal CNN (LPCNN) [22], which combined the proximal gradient method with CNN using COSMOS as the labels. MoDL-QSM [23] proposed a framework combining the STI physical model with a CNN using susceptibility tensor terms as labels. The above mentioed proximal gradient-based methods alternated CNN blocks and a steepest descent step. Apart from these above mentioned supervised methods, Fidelity imposed network edit (FINE) [32] method tuned the weights of the pre-trained network for each testing dataset via minimizing an unsupervised model loss function. However, these algorithms are also computationally expensive. In addition, an unsupervised approaches using adaptive instance normalization was proposed to reconstruct QSM images with various resolutions [33]. More recently, an end-to-end Affine Transformation Edited and Refined (AFTER) deep neural network was proposed for the inversion problem, which is robust to image acquisition orientations and resolutions [34].

Inspired by the model-based deep learning architecture for the inverse problem (MoDL) [35], this study aims to address a recursive neural network architecture involving the data consistency term and a CNN to solve the dipole inversion problem in QSM reconstruction. The proposed network alternates between the numerical optimization block, which encourages data consistency with the measured data, and a CNN block, which captures the information of the training data. For brevity, we refer to the proposed method as NoQSM-net. The numerical optimization algorithm used in the network was a conjugate gradient (CG) [36], which is the main difference from proximal gradient-based methods. Our experiments indicated that NoQSM-net improved the accuracy of susceptibility quantification compared with LPCNN and other methods.

II. THEORETICAL BACKGROUND

A. FORWARD PROBLEM FOR SUSCEPTIBILITY SOURCE TO MAGNETIC FIELD

In theory, the tissue field $b(r)$ located in r can be approximated as the convolution of susceptibility $\chi(r)$ with dipole kernel $d(r)$ in spatial domains. The forward problem from the susceptibility source to the tissue magnetic field can be expressed as follows:

$$b(r) = \frac{3cos^2\theta - 1}{4\pi r^3} \otimes \chi(\mathbf{r}) = d(\mathbf{r}) \otimes \chi(\mathbf{r})\,[r \neq 0]\,, \quad (1)$$

where $\otimes$ is the convolution operator and θ is the angle between $\mathbf{r}$ and the main magnetic field B_0. The matrix form of the forward problem can be written as a multiplication:

$$b = D\chi\,, \quad (2)$$

where b and χ denote the vector forms of the spatial susceptibility distribution and measured local field, respectively, and D is a matrix representing the convolution with dipole kernel $b(r) = \frac{3cos^2\theta-1}{4\pi r^3}$, which is defined as the magnetic field generated by a unit dipole. In k-space, susceptibility can be calculated by dividing the dipole D by the tissue field.

B. REGULARIZED OPTIMIZATION SCHEME FOR INVERSION

To estimate the susceptibility map χ from magnetic field measurement b is an ill-posed inverse problem, because of the zero cone surface of the dipole kernel when θ with respect to B_0 is $\pm 54.7°$ [19]. The regularized optimization method can be used to solve this inversion problem, which can be formulated as:

$$\chi(\mathbf{r}) = \underset{\chi}{argmin} \underbrace{\|W(b - D\chi)\|_2^2}_{weighted\ data\ fidelity} + \underbrace{\lambda R(\chi)}_{regularization}\,, \quad (3)$$

Here, the first item is to maintain data fidelity, and the second regularization prior is to restrict the solutions with the parameter λ.W is the square root of the inverse of the noise-covariance matrix. The first term of Equation (3) is the weighted data fidelity term, which contains artifact and noise; the second term is regularization term, which contains the regularization error. λ is a tunable regularization parameter, which is chosen such that the regularization error is approximately equal to the expected noise level. A wide range of classical forms for $RD_\omega(\chi)$have been researched, which include piece-wise constant susceptibility [37], [38], smooth susceptibility or susceptibility gradient [11], Wavelet [39], [40], and morphological consistency of the susceptibility map [15], [16], [17], [18]

III. PROPOSED METHOD

A. COMBINATION THE NUMERICAL OPTIMIZATION WITH CNN

The reconstruction of QSM maps can be formulated as the optimization problem:

$$\chi = \underset{\chi}{argmin} \|W(b - D\chi)\|_2^2 + \lambda \|\chi - RD_\omega(\chi)\|^2, \quad (4)$$

where, $RD_\omega(\chi)$ is the version of χ after artifact removal and denoising, which depends on the training parameters ω in CNN block. When the susceptibility map χ suffers from contamination by artifacts and noise, the CNN-based prior $\|\chi - RD_\omega(\chi)\|^2$ will yield high values. In addition, λ is set as the trainable regularization factor. If the constrained setting can yield an improved reconstruction, high values of λ are selected during the training process.

We can unroll the recursive network as follows: setting $\chi = \chi_n \pm \Delta\chi$ at n^{th} epoch iteration, and the nonlinear mapping $RD_\omega(\chi)$ can be approximated using a Taylor series around the nth iteration as:

$$RD_\omega(\chi) = RD_\omega(\chi_n \pm \Delta\chi) \approx \varphi_v + \mathbf{J}_n^T \Delta\chi, \quad (5)$$

where $\mathbf{J}_n$ is the Jacobian matrix, $\varphi_n = RD_\omega(\chi_n)$. Then the penalty term can be approximated as:

$$\|\chi - RD_\omega(\chi_n + \Delta\chi)\|^2 \approx |\chi - \varphi_n|^2 + \|\mathbf{J}_n \Delta\chi\|, \quad (6)$$

Note that the second term in Equation (6) tends to zero for a small value of $\|\Delta\chi\|$. Because the above approximation is only valid in the vicinity of χ_n, we can approximate the alternating algorithm as:

$$\chi_{n+1} = \underset{\chi}{argmin} \|W(b - D\chi)\|_2^2 + \lambda \|\chi - \varphi_n\|^2, \quad (7)$$

The solution of Equation (7) can be obtained using the normal equation:

$$\chi_{n+1} = \left((WD)^H (WD) + \lambda I\right)^{-1} \left((WD)^H (Wb) + \lambda\varphi_n\right), \quad (8)$$

Here, the $(\cdot)^H$ indicates conjugate transpose. The algorithm was initialized with $(WD)^H (Wb)$. The operator $\left((WD)^H (WD) + \lambda I\right)^{-1}$ is not analytically invertible for the inverse problem. The update of Equation (9) can be solved using CG [36] optimization scheme, which involves several CG steps. Furthermore, there are no trainable parameters within the CG sub-blocks. The outline of the alternating scheme is described in Fig. 1(b).

B. FRAMEWORK OF NOQSM-NET

The architecture of the NoQSM-net is illustrated in Fig. 1(a). The network used in the CNN block is shown in Fig. 1(c), which includes 18 convolutional layers. There are eight residual blocks and two convolution layers in the CNN. The kernel size of the first convolution layer and the convolution layers in the residual blocks was $3 \times 3 \times 3$, with stride 1 and channel 32. The last layer, with a kernel size of $1 \times 1 \times 1$ and 1 output, generates the predicted susceptibility of the CNN. Batch normalization (BN) [41] was used to accelerate convergence, and the rectified linear unit (ReLU) activation function [42] was applied to mitigate overfitting. The bottom of each output block summarizes the number of channels, and the top summarizes the size of the output.

IV. EXPERIMENTS

A. DATA FOR TRAINING AND TESTING

The multi-orientation GRE dataset used for training and testing in our study was downloaded from https://osf.io/y6rc3/ [43].

Training dataset: Our training data included 5 healthy volunteers with 15-23 head orientations per subject. The datasets were acquired by the multi-echo 3D GRE sequence with the following scan parameters: FOV = $210 \times 224 \times 160$ mm^3, voxel size = $1 \times 1 \times 1$ mm^3 isotropic, TR = 38 ms, TE1 = 7.7 ms, echo spacing = 5 ms, number of echoes = 6, bandwidth = 190 Hz/pixel, flip angle = 15°, GRAPPA factor = 2, and total imaging time = 8.8 s. The scan was repeated at different head orientations for each participant.

Testing dataset: 35 multiple head orientation scans from two healthy volunteers were acquired using the same scanner and imaging parameters as the training data. A patient with multiple sclerosis (MS) was used to explore the potential clinical applications. Patients with MS were acquired using a 3D GRE sequence on a 3T GE HDxt MR scanner with the following parameters: flip angle = 12°, matrix size = $256 \times 256 \times 124$, 1 mm isotropic resolution, TR = 32.36 ms, TE1/echo spacing = 3.2/2.4 ms, number of echoes = 12.

B. DATA PROCESSING

The masks of the brain were generated from magnitude data using BET in the FSL [44]. The phase images within the mask were spatially unwrapped using a Laplacian phase-unwrapping algorithm [45] and then processed by removing the background phase via V-SHARP [39]. The obtained tissue phase images of different echoes were normalized by $2\pi\gamma TEB_0$ and then averaged to generate local field maps, where γ is the gyromagnetic ratio, TE is the echo time,

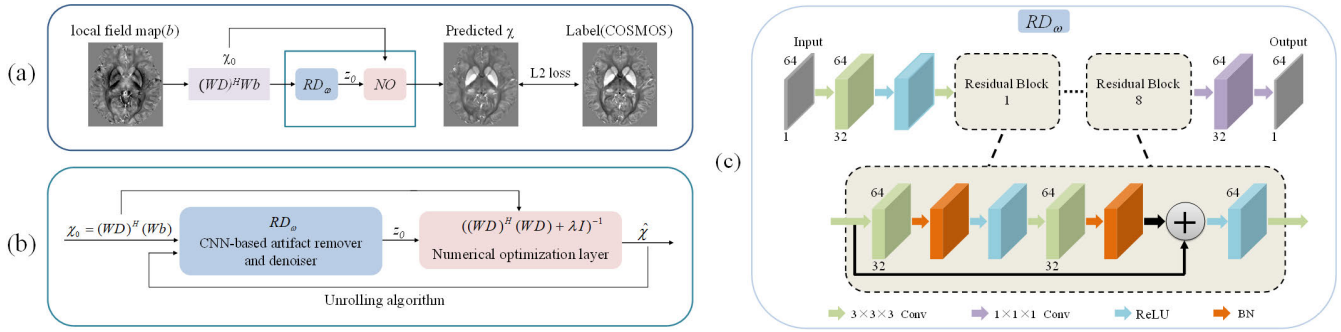

FIGURE 1. Overview of the proposed NoQSM-net architecture. (a) The schematic diagram of NoQSM-net. RD_ω represents the CNN block and NO is the numerical optimization block. (b) The recursive NoQSM-net framework that alternates between artifact remover and denoiser RD_ω and data consistency NO layer. (c) The network structure of residual CNN. The bottom of blocks summarizes the number of channels after each layer and the top of blocks summarizes the output size.

and B_0 is the main field strength. To reconstruct the reference susceptibility images of the multiple orientation data, the resulting local field maps were registered as follows. First, the other orientation magnitude images of the first echo were registered to that of the unrotated head orientation to calculate the rotation matrices using FSL FLIRT [46], [47]. The resulting rotation matrices are then applied to the corresponding local field maps for registration. Finally, the QSM maps were reconstructed using the registered local field maps using the COSMOS algorithm [19], which served as the label. A total of 94 scans of healthy volunteers were obtained for training.

C. IMPLEMENTATION DETAILS

The proposed unrolling model NoQSM-net was implemented using python 3.7.0 and Keras 2.6.0, with TensorFlow as the backend, on a 64-bit Windows 10 workstation (Intel Xeon CPU and 128 GB RAM). Training was accelerated using a graphics processing unit card (RTX A4000, Nvidia). To fit into the GPU memory, the patch size for NoQSM-net training was cropped to $64 \times 64 \times 64$ with an overlapping scheme of 66% between adjacent patches. To improve the training efficiency, patches with more than 40% background regions were discarded. A total of 7226 patches were obtained. Of these patches, 80% were used for training, and 20% for validation. During the training procedure, patches of size $64 \times 64 \times 64$ and the corresponding dipole kernel of full size were fed into the CNN. To preserve high-frequency information, $64 \times 64 \times 64$ patches were padded to the original size to match the size of the dipole kernel when performing the numerical optimization operator and then cropped back to $64 \times 64 \times 64$. The mean-squared error (MSE) was used as the loss function in the proposed method:

$$L = \|\chi_{recon} - \chi_{COSMOS}\|^2, \tag{9}$$

where the χ_{COSMOS} denotes the label susceptibility map, and χ_{recon} represents the reconstructed susceptibility map from NoQSM-net. The minimization of L_2 loss was performed using the Adam optimizer [48]. The initial learning rate was set to 10^{-3} and reduced by a factor of 0.5, when the validation loss did not decay in five epochs. The batch size was set to one because of the memory limitations of the GPU. The training was stopped early at 80 epochs, when the performance was stable. The total training time of NoQSM-net was approximately 58h.

We also develop how to back-propagate through these conjugate gradient (CG) block. We have

$$\nabla_\varphi L = \mathbf{J}_\varphi (\chi)^T \nabla_\chi L, \tag{10}$$

where the Jacobian matrix$\mathbf{J}_\varphi (\chi) = \left((WD)^H (WD) + \lambda I\right)^{-1}$. Since $(WD)^H (WD) + \lambda I$ is symmetric, we have

$$\nabla_\varphi L = \left((WD)^H (WD) + \lambda I\right)^{-1} \nabla_\chi L, \tag{11}$$

Equation (11) thus indicates that the gradients can be back-propagated through the CG block using a CG algorithm, which means the CG block do not have trainable parameters.

D. PERFORMANCE EVALUATION

In this study, we also compared the approach that used the steepest descent (SD) optimization algorithm instead of CG in the numerical optimization sub-block, which is abbreviated as NoQSM-SD. The proposed method using the CG sub-block is abbreviated as NoQSM-CG. We evaluated the performance of the NoQSM-net in two healthy subjects with 35 head orientations. The images reconstructed by COSMOS were used as the reference images. In addition, the proposed method was compared with the MEDI, QSMnet, and LPCNN methods. Among them, the regularization factor of the single-orientation QSM calculated using the MEDI algorithm was set to 3000 [17]. The structure similarity index (SSIM) [49], peak signal-to-noise ratio (PSNR), normalized root mean squared error (NRMSE), and high-frequency error norm (HFEN) were calculated for a global quantitative comparison. We also compared the visual performance of healthy subjects using these different methods. And we also developed the quantitative performance of different iteration numbers in CG sub-block.

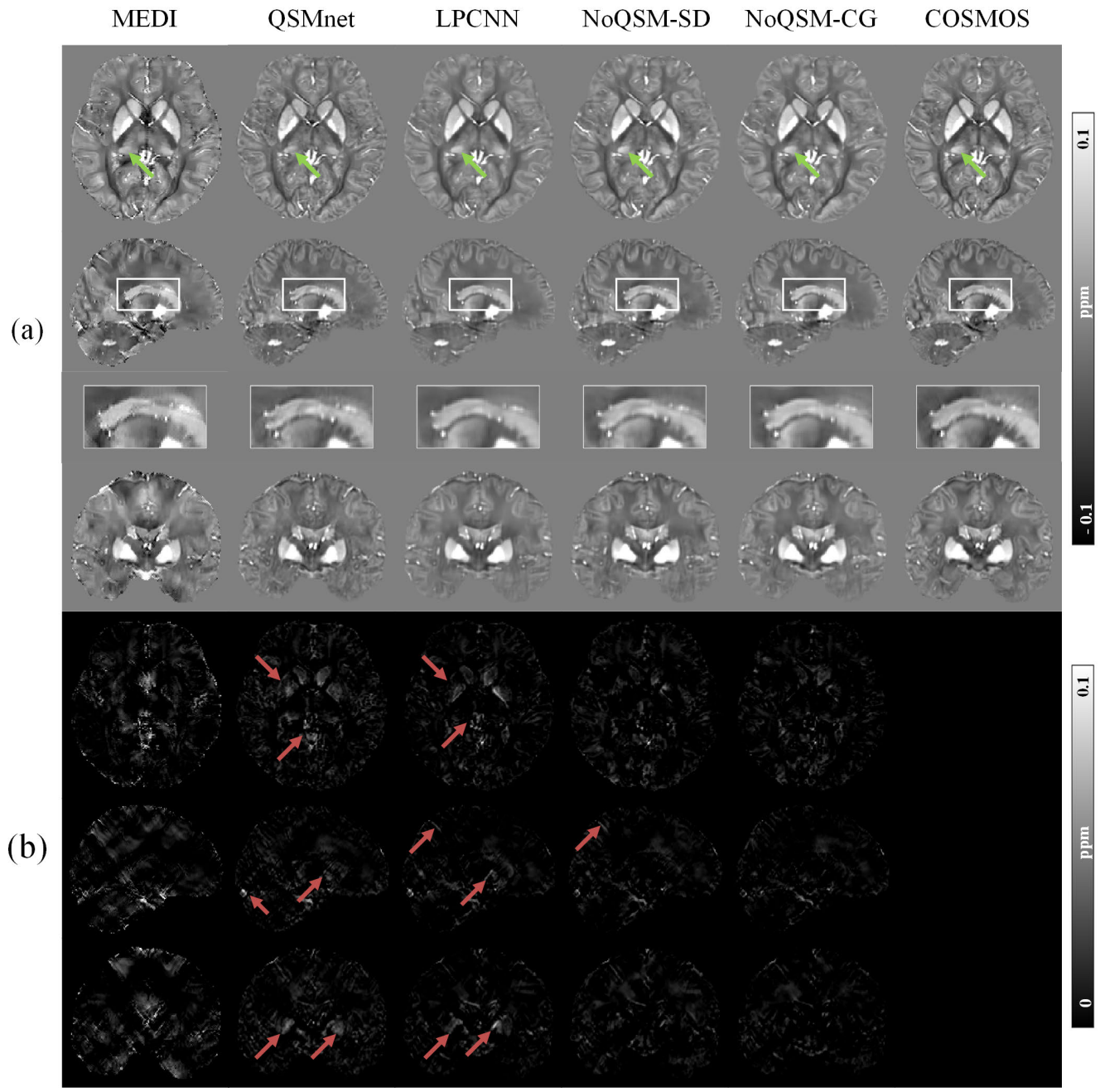

FIGURE 2. Comparision of the QSM images of a representative subject reconstructed by MEDI, QSMnet, LPCNN, NoQSM-SD and NoQSM-CG. (a) The three orthogonal views of the reconstructed QSM maps are displayed in the first, second and forth row, the third row is the zoomed-in maps of the outlined white box. (b) The residual maps of the three orthogonal views between different reconstruction results and COSMOS maps. Red arrows indicate regions with larger differences on QSMnet, LPCNN and NoQSM-SD maps.

We performed the region of interest (ROI) analysis in the putamen (PUT) and globus pallidus (GP) to further demonstrate the quantitative accuracy of NoQSM-net in deep gray matter. Then, the mean and standard deviation of the susceptibility reconstructed by different methods are displayed in the selected ROI. In addition, to study potential clinical applications, the QSM images of MS data reconstructed by QSMnet, LPCNN, and NoQSM-net were compared by visual inspection.

V. RESULTS

Fig. 2 shows three orthogonal views of the QSM images and the corresponding error maps from a representative healthy test dataset reconstructed using different methods. The first row of Fig. 2(a) shows axial views of the different methods. As indicated by the green arrows, NoQSM-CG and NoQSM-SD displayed more similarity to the COSMOS maps. The second and third images in Fig. 2(a) show the sagittal plane and the zoomed-in view of the region outlined by the

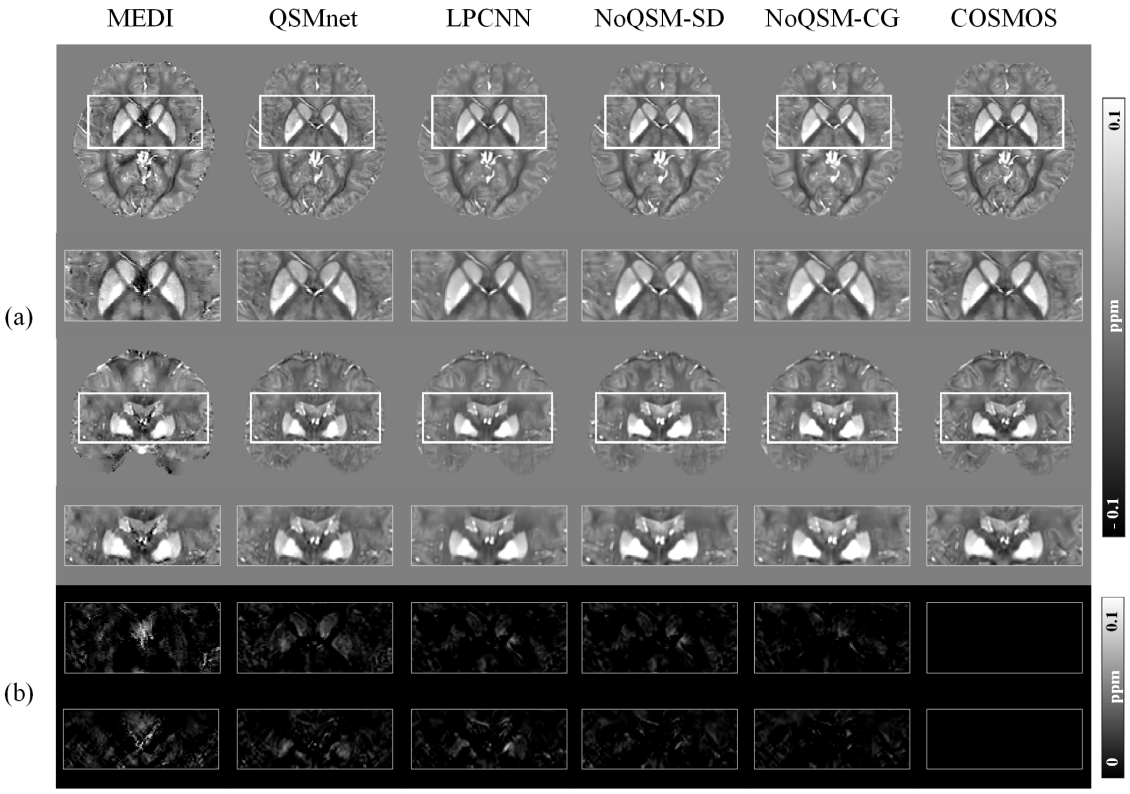

FIGURE 3. Axial and coronal views of the QSM maps of the subject in Fig. 2. (a) The axial and coronal views are displayed in the first and third row; the zoomed-in views of the region outlined by the white box are showed in the second and forth row. (b) The zoomed-in difference maps. NoQSM-net shows smaller errors relative to the label than the other compared methods.

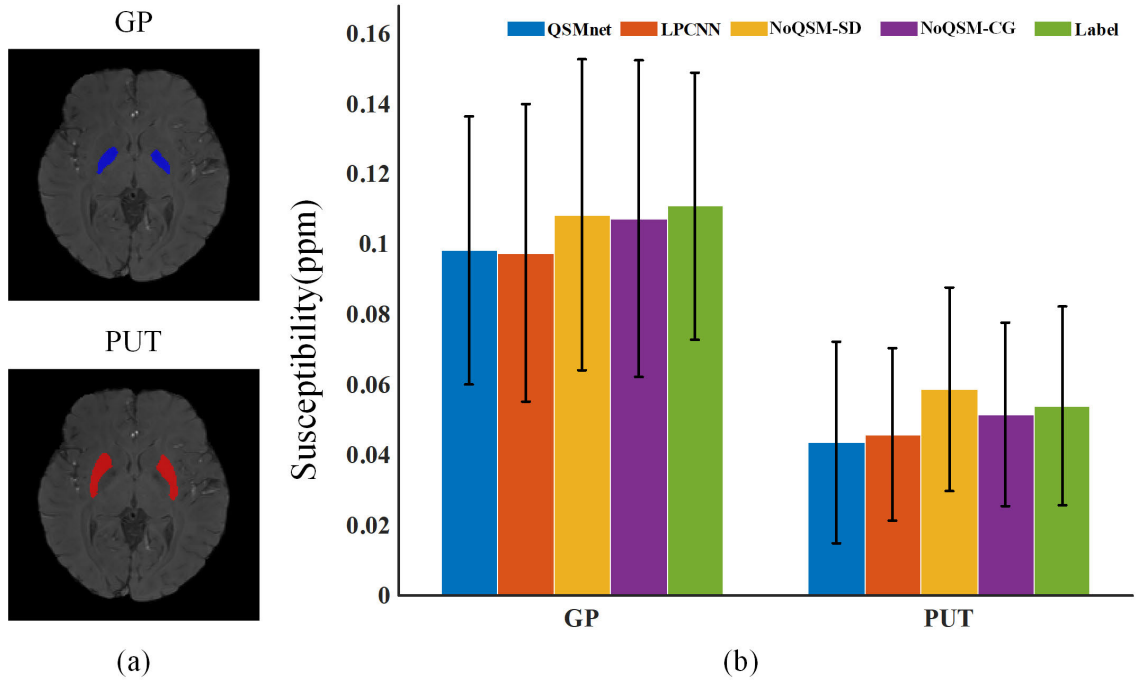

FIGURE 4. Quantitative analysis of the susceptibility values in globus pallidus (GP) and putamen (PUT). (a) The blue region of interest on the magnitude image is the GP, the red is PUT. (b) The susceptibility values in the GP and PUT. Data are presented as mean ± standard deviation. The result of proposed NoQSM-CG matches well with the COSMOS.

white box. The coronal views are displayed in the fourth row of Fig. 2(a). Fig. 2 (b) illustrates the error maps, QSMnet and MEDI show larger differences and more artifacts. As the red arrows show, compared with LPCNN and NoQSM-SD,

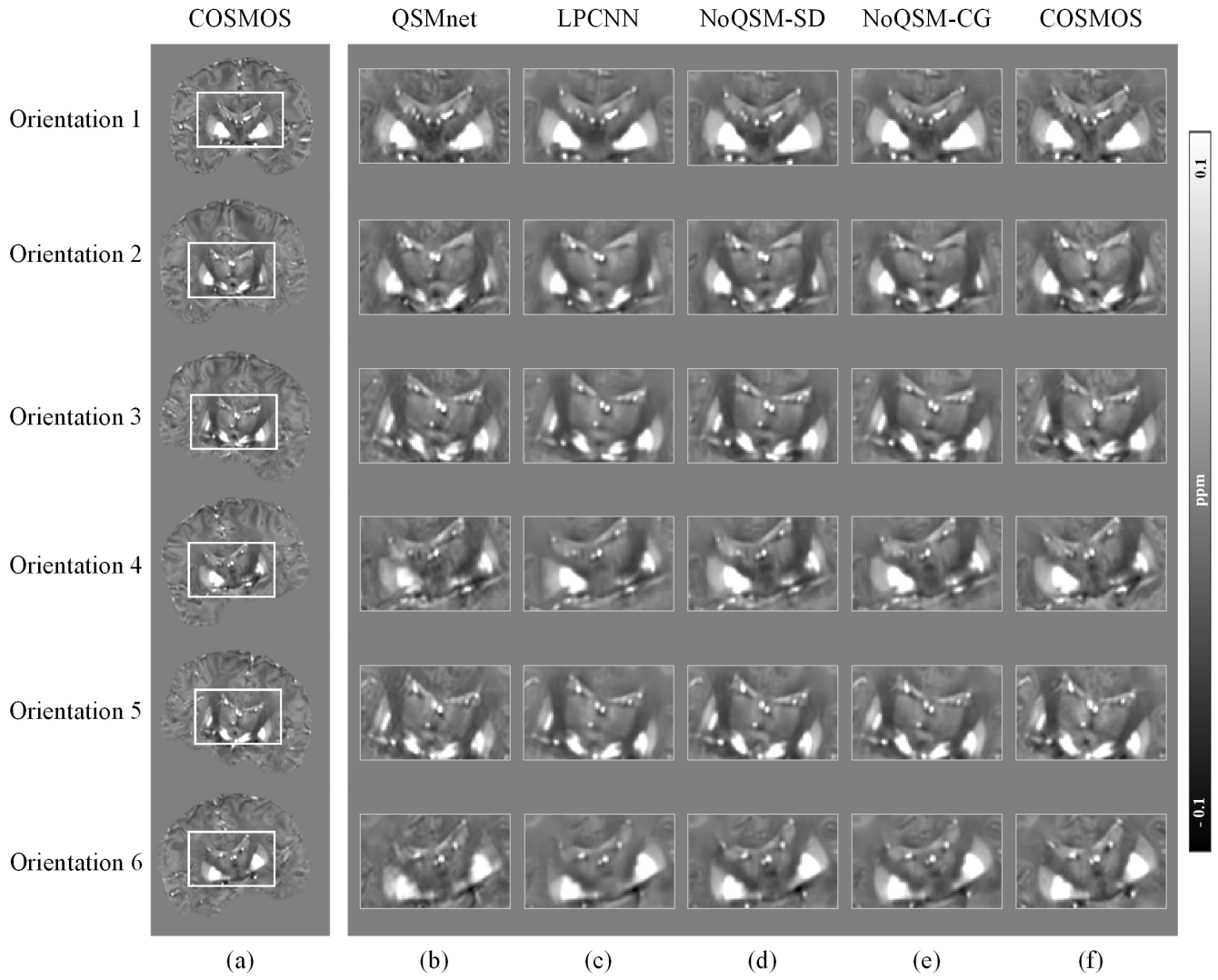

FIGURE 5. The zoomed-in axial views of the other subject in different head orientation. (a) and (f) Different head orientation COSMOS maps and the corresponding zoomed-in maps. (b-e) The multi-orientation zoomed-in QSM maps reconstructed by QSMnet, LPCNN, NoQSM-SD and NoQSM-CG. NoQSM-net shows more accurate estimation than the other deep learning methods.

NoQSM-CG yields fewer residuals. NoQSM-net, especially NoQSM-CG, yielded fewer streaking artifacts than the other methods.

Fig. 3 describes the axial and coronal (Fig. 3 (a) and Fig. 3 (b)) views of the reconstructed QSM images in Fig. 2. The zoomed-in images of the region outlined by the white box are displayed in the second and fourth rows of Fig. 3 (a), and the corresponding zoomed-in residual maps are displayed in Fig. 3 (b). Compared with the MEDI, QSMnet, and LPCNN methods, the NoQSM-net method, especially the NoQSM-CG, produced more accurate susceptibility estimation and fewer residuals in certain brain regions, such as veins, nucleus accumbens, caudate nucleus, putamen (PUT), and globus pallidus (GP).

Regions of interest were selected to analyze the reconstructed efficacy of these deep learning-based methods. Fig. 4 shows a comparison of the reconstructed regional susceptibility values in the deep nuclei. Two typical regions of interest, namely GP (blue region in the first row of Fig. 4(a)) and PUT (red region in the second row of Fig. 4 (a)), were selected. Fig. 4 (b) displays the susceptibility values of GP and PUT. Compared with labels, NOQSM-SD shows better estimations in GP but over-estimations in PUT. Meanwhile, QSMnet and LPCNN illustrate underestimated susceptibility values in both selected regions. In contrast, NoQSM-CG has better susceptibility estimations for both GP and PUT.

Fig. 5 illustrates the coronal views of six different head orientations from the other representative healthy subjects. Fig. 5 (a) and (f) show the COSMOS maps and the corresponding zoomed-in maps for different head orientations. Fig. 5 (b-e) display zoomed-in views of the region outlined by the white box in Fig. 5 (a) from different deep learning-based methods. In comparison with QSMnet and LPCNN,

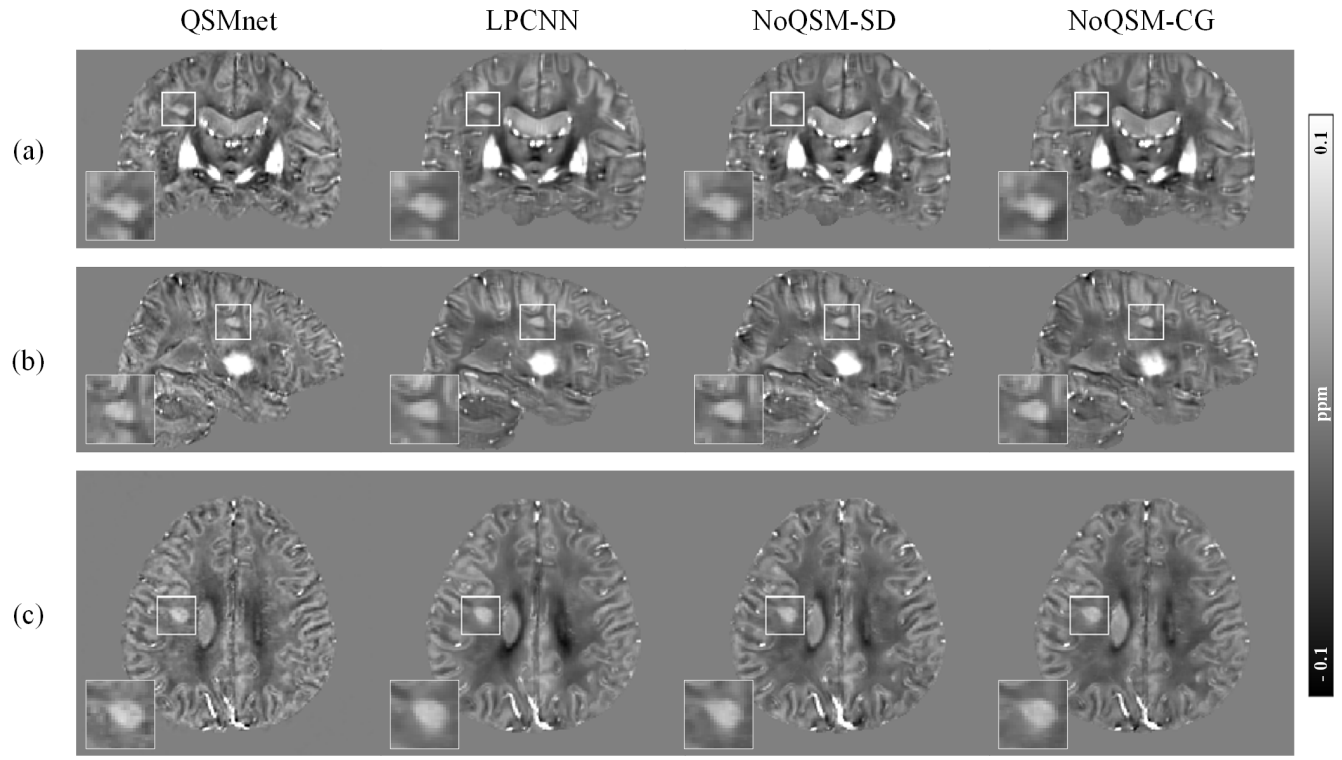

FIGURE 6. The application to a MS patient of different deep learning based methods. Three orthogonal views and the zoomed-in views show that these methods can all detect the lesion region.

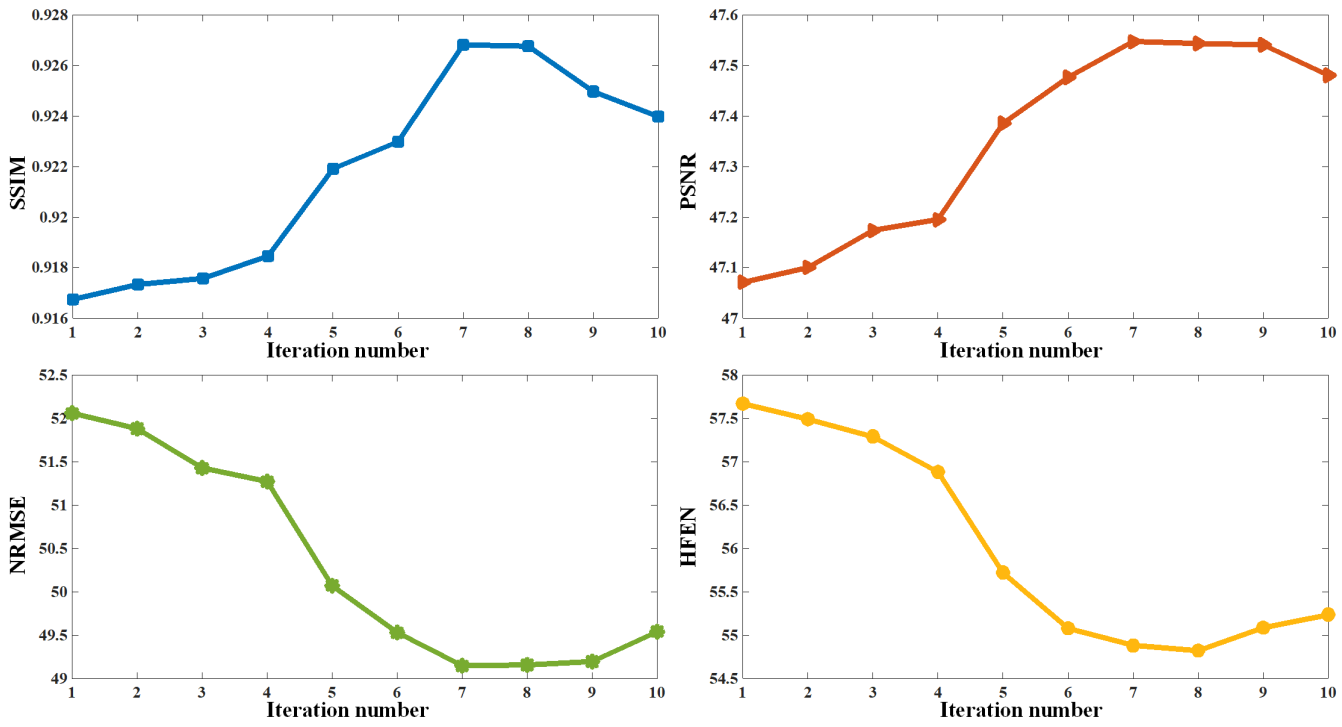

FIGURE 7. The SSIM, PSNR, NRMSE and HFEN resulst of different iterations in CG sub-block.

the reconstructed QSM images of NoQSM-net show less blurry and fewer streaking artifacts in each orientation.

Fig. 6 presents the application of QSMnet, LPCNN, and NoQSM-net to an MS patient. The three orthogonal views

TABLE 1. The quantitative evaluation of MEDI, QSMnet, LPCNN, NoQSM-SD and NoQSM-CG in terms of SSIM, PSNR, NRMSE and HFEN. The proposed NoQSM-CG shows the best metrics in all methods.

	SSIM	NRMSE%	HFEN%	PSNR
MEDI	0.863 ± 0.031	117.23 ± 22.55	114.58 ± 24.81	40.19 ± 1.65
QSMnet	0.881 ± 0.038	61.97 ± 11.63	68.73 ± 13.28	45.65 ± 1.48
LPCNN	0.917 ± 0.021	51.31 ± 7.07	56.40 ± 8.29	47.22 ± 1.05
NoQSM-SD	0.924 ± 0.010	49.53 ± 3.59	55.11 ± 4.04	47.47 ± 0.52
NoQSM-CG	$\mathbf{0.927 \pm 0.011}$	$\mathbf{49.16 \pm 3.46}$	$\mathbf{54.83 \pm 4.02}$	$\mathbf{47.54 \pm 0.51}$

and the corresponding zoomed-in images of the outlined white box are demonstrated in Fig. 6 (a-c). All deep-learning-based QSM reconstruction methods can detect lesion regions. The lesion area was similarly delineated in all methods.

Fig. 7 shows the quantitative metrics of different CG iterations in the proposed alternating algorithm. The SSIM, PSNR, NRMSE and HFEN indicates that while CG iteration is set to 7, NoQSM-net can achieve the optimal quantitative performance.

Table 1 presents the quantitative metrics SSIM, PSNR, NRMSE, and HFEN of the different methods. The results of NoQSM-CG achieved the highest SSIM with 0.927 and PSNR with 47.54, and the lowest NRMSE with 49.16 and HFEN with 54.83, suggesting the best performance based on these quantitative criteria.

VI. DISCUSSION

In this study, we developed an unrolling deep learning algorithm consisting of a data consistency block and a CNN block to solve ill-posed dipole inversion problem in QSM reconstruction. Data consistency was enforced by using the numerical optimization blocks, that is, the SD and CG blocks within the network. The CNN block used in the unrolling model was a residual network. Our results indicate that the proposed NoQSM-net method could effectively suppress the streaking artifact caused by the noise amplification effect from the division of dipole kernel values close to 0 in the dipole deconvolution, and the error maps show that the predicted QSM images are close to the golden standard COSMOS maps.

Several unrolled methods have been proposed, such as VaNDI [31], LPCNN [22] and MoDL-QSM [23]. Compared to the use of a CNN as one of the regularization terms in Eq. (4) for artifact removal and denoising, VaNDI trained the variational network to optimize the parameters in an iterative gradient descent algorithm. The main difference between the LPCNN and the proposed method is that the latter incorporates a CNN into the proximal gradient descent algorithm by learning the associated proximity operator. The proposed method alternated between the numerical optimization block (i.e., the CG sub-block) and the CNN. MoDL-QSM, which was combined with the STI model, used the susceptibility tensor as labels. In addition, the framework of MoDL-QSM and LPCNN was similar. The proposed method and LPCNN both used COSMOS as labels; therefore, we only compared the LPCNN method with the method proposed in this paper. The use of the CG sub-block in our approach led to more accurate enforcement of the data consistency constraint and enabled the easy use of the forward model, thus offering a faster cost reduction. And our results indicate that the proposed NoQSM-net is superior to the LPCNN.

The results in Fig. 2 Fig. 3 and the quantitative metrics indicate that NoQSM-CG was slightly superior to NoQSM-SD. In contrast, NoQSM-CG achieves a more accurate estimation than the LPCNN and QSMnet. The proposed method provides a much more accurate prediction than MEDI, which used the same CG optimization algorithm. The ROI analysis in Fig. 4 and the multi-orientation predictions in Fig. 5 demonstrate that NoQSM-CG matches well with the labels. In Fig. 6, the LPCNN, NoQSM-SD, and NoQSM-CG visibly detect the lesion regions in the MS data. However, the results of QSMnet are more blurred than those of the other methods. In addition, the quantitative results in Table 1 indicate that quantitative metrics of the proposed method were the best compared with the other methods. In addition, we also studied the iteration number in CG sub-block by calculating the SSIM, PSNR, NRMSE and HFEN of different CG iteration numbers, which displayed in Fig. 7. Considering the memory, training time and performance, the number of CG iteration was set to 7 during training.

This study has several limitations that can be addressed in the future. First, the regularization term in the proposed method can be replaced by piecewise constant susceptibility [37], total variation (TV) [50], etc.. Second, when the iteration number was set to 2 or 3, the training time would be increased to 110 h and 210 h. So the iteration number was set to one in this study when considering the time costs. In the future, the number of iterations can be increased. Finally, the CNN block used in our method was a residual network. We can replace the residual network with the Unet or other networks.

VII. CONCLUSION

We propose a network combining CNN and numerical optimization algorithm to solve the ill-posed dipole inversion problem in single-orientation QSM reconstruction. The COSMOS maps are used as labels. The proposed NoQSM-net can improve the susceptibility quantification performance by simultaneously using additional priors and suppressing streaking artifacts. Our experimental results show that reconstructed QSM images by NoQSM-net yield superior accuracy and fewer artifacts and noise than other methods in healthy subjects. In addition, NoQSM-net can characterize the lesions in the MS data well.

REFERENCES

[1] Y. Wang et al., "Clinical quantitative susceptibility mapping (QSM): Biometal imaging and its emerging roles in patient care," *J. Magn. Reson. Imag.*, vol. 46, no. 4, pp. 951–971, Oct. 2017.

[2] P. P. R. Ruetten, J. H. Gillard, and M. J. Graves, "Introduction to quantitative susceptibility mapping and susceptibility weighted imaging," *Brit. J. Radiol.*, vol. 92, no. 1101, Sep. 2019, Art. no. 20181016.

[3] J. Acosta-Cabronero, G. B. Williams, A. Cardenas-Blanco, R. J. Arnold, V. Lupson, and P. J. Nestor, "In vivo quantitative susceptibility mapping (QSM) in Alzheimer's disease," *PLoS ONE*, vol. 8, no. 11, Nov. 2013, Art. no. e81093.

[4] C. Langkammer, T. Liu, M. Khalil, C. Enzinger, M. Jehna, S. Fuchs, F. Fazekas, Y. Wang, and S. Ropele, "Quantitative susceptibility mapping in multiple sclerosis," *Radiology*, vol. 267, no. 2, pp. 551–559, May 2013.

[5] J. M. G. Van Bergen, J. Hua, P. G. Unschuld, I. A. L. Lim, C. K. Jones, R. L. Margolis, C. A. Ross, P. C. M. van Zijl, and X. Li, "Quantitative susceptibility mapping suggests altered brain iron in premanifest Huntington disease," *Amer. J. Neuroradiol.*, vol. 37, no. 5, pp. 789–796, 2016.

[6] X. Guan, P. Huang, Q. Zeng, C. Liu, H. Wei, M. Xuan, Q. Gu, X. Xu, N. Wang, X. Yu, X. Luo, and M. Zhang, "Quantitative susceptibility mapping as a biomarker for evaluating white matter alterations in Parkinson's disease," *Brain Imag. Behav.*, vol. 13, no. 1, pp. 220–231, 2019.

[7] J. Klohs, A. Deistung, F. Schweser, J. Grandjean, M. Dominietto, C. Waschkies, R. M. Nitsch, I. Knuesel, J. R. Reichenbach, and M. Rudin, "Detection of cerebral microbleeds with quantitative susceptibility mapping in the ArcAbeta mouse model of cerebral amyloidosis," *J. Cerebral Blood Flow Metabolism*, vol. 31, no. 12, pp. 2282–2292, 2011.

[8] T. Liu, K. Surapaneni, M. Lou, L. Cheng, P. Spincemaille, and Y. Wang, "Cerebral microbleeds: Burden assessment by using quantitative susceptibility mapping," *Radiology*, vol. 262, no. 1, pp. 269–278, Jan. 2012.

[9] W. Chen, W. Zhu, I. I. Kovanlikaya, A. Kovanlikaya, T. Liu, S. Wang, C. Salustri, and Y. Wang, "Intracranial calcifications and hemorrhages: Characterization with quantitative susceptibility mapping," *Radiology*, vol. 270, no. 2, pp. 496–505, 2014.

[10] S. Chang, J. Zhang, T. Liu, A. J. Tsiouris, J. Shou, T. Nguyen, D. Leifer, Y. Wang, and I. Kovanlikaya, "Quantitative susceptibility mapping of intracerebral hemorrhages at various stages," *J. Magn. Reson. Imag.*, vol. 44, no. 2, pp. 420–425, Aug. 2016.

[11] B. Kressler, L. de Rochefort, T. Liu, P. Spincemaille, Q. Jiang, and Y. Wang, "Nonlinear regularization for per voxel estimation of magnetic susceptibility distributions from MRI field maps," *IEEE Trans. Med. Imag.*, vol. 29, no. 2, pp. 273–281, Feb. 2010.

[12] F. Schweser, A. Deistung, B. W. Lehr, and J. R. Reichenbach, "Quantitative imaging of intrinsic magnetic tissue properties using MRI signal phase: An approach to in vivo brain iron metabolism?" *NeuroImage*, vol. 54, no. 4, pp. 2789–2807, Feb. 2011.

[13] K. Shmueli, J. A. de Zwart, P. van Gelderen, T. Q. Li, S. J. Dodd, and J. H. Duyn, "Magnetic susceptibility mapping of brain tissue in vivo using MRI phase data," *Magn. Reson. Med.*, vol. 62, no. 6, pp. 1510–1522, Dec. 2009.

[14] B. Bilgic, A. P. Fan, J. R. Polimeni, S. F. Cauley, M. Bianciardi, E. Adalsteinsson, L. L. Wald, and K. Setsompop, "Fast quantitative susceptibility mapping with L1-regularization and automatic parameter selection," *Magn. Reson. Med.*, vol. 72, no. 5, pp. 1444–1459, Nov. 2014.

[15] L. de Rochefort, T. Liu, B. Kressler, J. Liu, P. Spincemaille, V. Lebon, J. Wu, and Y. Wang, "Quantitative susceptibility map reconstruction from MR phase data using Bayesian regularization: Validation and application to brain imaging," *Magn. Reson. Med.*, vol. 63, no. 1, pp. 194–206, Jan. 2010.

[16] J. Liu, T. Liu, L. de Rochefort, J. Ledoux, I. Khalidov, W. Chen, A. J. Tsiouris, C. Wisnieff, P. Spincemaille, M. R. Prince, and Y. Wang, "Morphology enabled dipole inversion for quantitative susceptibility mapping using structural consistency between the magnitude image and the susceptibility map," *NeuroImage*, vol. 59, no. 3, pp. 2560–2568, Feb. 2012.

[17] T. Liu, J. Liu, L. De Rochefort, P. Spincemaille, I. Khalidov, J. R. Ledoux, and Y. Wang, "Morphology enabled dipole inversion (MEDI) from a single-angle acquisition: Comparison with COSMOS in human brain imaging," *Magn. Reson. Med.*, vol. 66, no. 3, pp. 777–783, Sep. 2011.

[18] F. Schweser, K. Sommer, A. Deistung, and J. R. Reichenbach, "Quantitative susceptibility mapping for investigating subtle susceptibility variations in the human brain," *NeuroImage*, vol. 62, no. 3, pp. 2083–2100, Sep. 2012.

[19] T. Liu, P. Spincemaille, L. de Rochefort, B. Kressler, and Y. Wang, "Calculation of susceptibility through multiple orientation sampling (COSMOS): A method for conditioning the inverse problem from measured magnetic field map to susceptibility source image in MRI," *Magn. Reson. Med.*, vol. 61, no. 1, pp. 196–204, Jan. 2009.

[20] S. Wharton and R. Bowtell, "Whole-brain susceptibility mapping at high field: A comparison of multiple- and single-orientation methods," *NeuroImage*, vol. 53, no. 2, pp. 515–525, Nov. 2010.

[21] J. Yoon, E. Gong, I. Chatnuntawech, B. Bilgic, J. Lee, W. Jung, J. Ko, H. Jung, K. Setsompop, G. Zaharchuk, E. Y. Kim, J. Pauly, and J. Lee, "Quantitative susceptibility mapping using deep neural network: QSMnet," *NeuroImage*, vol. 179, pp. 199–206, Oct. 2018.

[22] K. W. Lai, M. Aggarwal, P. van Zijl, X. Li, and J. Sulam, "Learned proximal networks for quantitative susceptibility mapping," in *Proc. Int. Conf. Med. Image Comput. Comput.-Assist. Intervent. (MICCAI)*, vol. 12262, Oct. 2020, pp. 125–135.

[23] R. Feng, J. Zhao, H. Wang, B. Yang, J. Feng, Y. Shi, M. Zhang, C. Liu, Y. Zhang, J. Zhuang, and H. Wei, "MoDL-QSM: Model-based deep learning for quantitative susceptibility mapping," *NeuroImage*, vol. 240, Oct. 2021, Art. no. 118376.

[24] Y. Chen, A. Jakary, S. Avadiappan, C. P. Hess, and J. M. Lupo, "QSMGAN: Improved quantitative susceptibility mapping using 3D generative adversarial networks with increased receptive field," *NeuroImage*, vol. 207, Feb. 2020, Art. no. 116389.

[25] W. Jung, J. Yoon, S. Ji, J. Y. Choi, J. M. Kim, Y. Nam, E. Y. Kim, and J. Lee, "Exploring linearity of deep neural network trained QSM: QSMnet^{+}," *NeuroImage*, vol. 211, May 2020, Art. no. 116619.

[26] S. Bollmann, K. G. B. Rasmussen, M. Kristensen, R. G. Blendal, L. R. Østergaard, M. Plocharski, K. O'Brien, C. Langkammer, A. Janke, and M. Barth, "DeepQSM—Using deep learning to solve the dipole inversion for quantitative susceptibility mapping," *NeuroImage*, vol. 195, pp. 373–383, Jul. 2019.

[27] Z. Li, J. Li, C. Wang, Z. Lu, J. Wang, H. He, and J. Shi, "Meta-learning based interactively connected clique U-Net for quantitative susceptibility mapping," *IEEE Trans. Comput. Imag.*, vol. 7, pp. 1385–1399, 2021.

[28] Z. Lu, J. Li, C. Wang, R. Ge, L. Chen, H. He, and J. Shi, "S2Q-Net: Mining the high-pass filtered phase data in susceptibility weighted imaging for quantitative susceptibility mapping," *IEEE J. Biomed. Health Informat.*, vol. 26, no. 8, pp. 3938–3949, Aug. 2022.

[29] Y. Gao, X. Zhu, B. A. Moffat, R. Glarin, A. H. Wilman, G. B. Pike, S. Crozier, F. Liu, and H. Sun, "xQSM: Quantitative susceptibility mapping with octave convolutional and noise-regularized neural networks," *NMR Biomed.*, vol. 34, no. 3, p. e4461, Mar. 2021.

[30] H. Wei, S. Cao, Y. Zhang, X. Guan, F. Yan, K. W. Yeom, and C. Liu, "Learning-based single-step quantitative susceptibility mapping reconstruction without brain extraction," *NeuroImage*, vol. 202, Nov. 2019, Art. no. 116064.

[31] D. Polak, I. Chatnuntawech, J. Yoon, S. S. Iyer, C. Milovic, J. Lee, P. Bachert, E. Adalsteinsson, K. Setsompop, and B. Bilgic, "Nonlinear dipole inversion (NDI) enables robust quantitative susceptibility mapping (QSM)," *NMR Biomed.*, vol. 33, no. 12, p. e4271, Dec. 2020.

[32] J. Zhang, Z. Liu, S. Zhang, H. Zhang, P. Spincemaille, T. D. Nguyen, M. R. Sabuncu, and Y. Wang, "Fidelity imposed network edit (FINE) for solving ill-posed image reconstruction," *NeuroImage*, vol. 211, May 2020, Art. no. 116579.

[33] G. Oh, H. Bae, H.-S. Ahn, S.-H. Park, W.-J. Moon, and J. C. Ye, "Unsupervised resolution-agnostic quantitative susceptibility mapping using adaptive instance normalization," *Med. Image Anal.*, vol. 79, Jul. 2022, Art. no. 102477.
[34] Z. Xiong, Y. Gao, F. Liu, and H. Sun, "Affine transformation edited and refined deep neural network for quantitative susceptibility mapping," *NeuroImage*, vol. 267, Feb. 2023, Art. no. 119842.
[35] H. K. Aggarwal, M. P. Mani, and M. Jacob, "MoDL: Model-based deep learning architecture for inverse problems," *IEEE Trans. Med. Imag.*, vol. 38, no. 2, pp. 394–405, Feb. 2019.
[36] M. R. Hestenes and E. Stiefel, "Methods of conjugate gradients for solving linear systems," *J. Res. Nat. Bureau Standards*, vol. 49, no. 6, pp. 409–436, 1952.
[37] L. de Rochefort, R. Brown, M. R. Prince, and Y. I. Wang, "Quantitative MR susceptibility mapping using piece-wise constant regularized inversion of the magnetic field," *Magn. Reson. Med.*, vol. 60, no. 4, pp. 1003–1009, Oct. 2008.
[38] F. Schweser, A. Deistung, B. W. Lehr, and J. R. Reichenbach, "Differentiation between diamagnetic and paramagnetic cerebral lesions based on magnetic susceptibility mapping," *Med. Phys.*, vol. 37, no. 10, pp. 5165–5178, Oct. 2010.
[39] B. Wu, W. Li, A. Guidon, and C. Liu, "Whole brain susceptibility mapping using compressed sensing," *Magn. Reson. Med.*, vol. 67, no. 1, pp. 137–147, Jan. 2012.
[40] B. Bilgic, A. Pfefferbaum, T. Rohlfing, E. V. Sullivan, and E. Adalsteinsson, "MRI estimates of brain iron concentration in normal aging using quantitative susceptibility mapping," *NeuroImage*, vol. 59, no. 3, pp. 2625–2635, Feb. 2012.
[41] S. Ioffe and C. Szegedy, "Batch normalization: Accelerating deep network training by reducing internal covariate shift," in *Proc. Int. Conf. Mach. Learn.*, 2015, pp. 448–456.
[42] V. Nair and G. E. Hinton, "Rectified linear units improve restricted Boltzmann machines," in *Proc. 27th Int. Conf. Mach. Learn.*, 2010, pp. 807–814.
[43] Y. Shi, R. Feng, Z. Li, J. Zhuang, Y. Zhang, and H. Wei, "Towards in vivo ground truth susceptibility for single-orientation deep learning QSM: A multi-orientation gradient-echo MRI dataset," *NeuroImage*, vol. 261, Nov. 2022, Art. no. 119522.
[44] S. M. Smith, "Fast robust automated brain extraction," *Hum. Brain Mapping*, vol. 17, no. 3, pp. 143–155, Nov. 2002.
[45] M. A. Schofield and Y. Zhu, "Fast phase unwrapping algorithm for interferometric applications," *Opt. Lett.*, vol. 28, no. 14, pp. 1194–1196, Jul. 2003.
[46] M. Jenkinson and S. Smith, "A global optimisation method for robust affine registration of brain images," *Med. Image Anal.*, vol. 5, no. 2, pp. 143–156, Jun. 2001.
[47] M. Jenkinson, "Improved optimization for the robust and accurate linear registration and motion correction of brain images," *NeuroImage*, vol. 17, no. 2, pp. 825–841, Oct. 2002.
[48] D. P. Kingma and J. Ba, "Adam: A method for stochastic optimization," 2014, *arXiv:1412.6980*.
[49] Z. Wang, A. C. Bovik, H. R. Sheikh, and E. P. Simoncelli, "Image quality assessment: From error visibility to structural similarity," *IEEE Trans. Image Process.*, vol. 13, no. 4, pp. 600–612, Apr. 2004.
[50] D.-Q. Chen and L.-Z. Cheng, "Spatially adapted total variation model to remove multiplicative noise," *IEEE Trans. Image Process.*, vol. 21, no. 4, pp. 1650–1662, Apr. 2012.

QIANQIAN ZHANG received the B.Eng. degree from Henan University of Science and Technology, in 2013. She is currently pursuing the Ph.D. degree with Guangdong Provincial Key Laboratory of Medial Image Processing, School of Biomedical Engineering, Southern Medical University. Her research interests include MRI image analysis, deep learning, and MRI image reconstruction.

YIHAO GUO received the B.S. and Ph.D. degrees from the Department of Biomedical Engineering, Southern Medical University, Guangzhou, China, in 2015 and 2020, respectively. His research interest include MRI image analysis and MRI image processing.

WUFAN CHEN (Senior Member, IEEE) received the B.S. and Ph.D. degrees from Beihang University, in 1975 and 1981, respectively. From 1981 to 1987, he was with the School of Aerospace, National University of Defense Technology, China. From 1987 to 2004, he was with the Department of Training, First Military Medical University, China. Since 2004, he has been with Southern Medical University.